Hierarchical Double-Shell Nanostructures of TiO_2 Nanosheets on SnO_2 Hollow Spheres for High-Efficiency, Solid-State, Dye-Sensitized Solar Cells

*Sung Hoon Ahn, Dong Jun Kim, Won Seok Chi, and Jong Hak Kim**

A high-energy conversion efficiency of 8.2% at 100 mW cm^{-2} is reported, one of the highest values for N719-based, solid-state, dye-sensitized solar cells (ssDSSCs). The solar cells are based on hierarchical double-shell nanostructures consisting of inner SnO_2 hollow spheres (SHS) surrounded by outer TiO_2 nanosheets (TNSs). Deposition of the TNS on the SHS outer surface is performed via solvothermal reactions in order to generate a double-shell SHS@TNS nanostructure that provides a large surface area and suppresses recombination of photogenerated electrons. An organized mesoporous (OM)-TiO_2 film with high porosity, large pores, and good interconnectivity is also prepared via a sol-gel process using a poly(vinyl chloride)-g-poly(oxyethylene methacrylate) (PVC-g-POEM) graft copolymer template. This film is utilized as a matrix to disperse the double-shell nanostructures. Such nanostructures provide good pore-filling for solid polymer electrolytes, faster electron transfer, and enhanced light scattering, as confirmed by reflectance spectroscopy, incident photon-to-electron conversion efficiency (IPCE), and intensity-modulated photocurrent spectroscopy (IMPS)/intensity-modulated photovoltage spectroscopy (IMVS).

1. Introduction

Since O'Regan and Gratzel introduced dye-sensitized solar cells (DSSCs),[1] interest in DSSCs has intensified due to their low production cost, high efficiency, green production process, and ease of fabrication. The energy conversion efficiency of DSSCs can be improved by developing or modifying each component, including sensitizers,[2,3] electrolytes,[4–6] photoanodes,[7–9] and counter electrodes.[10–13] Although efficiency reaching 12% has been recorded for DSSCs with organic liquid electrolytes, these DSSCs are ineffective for outdoor applications due to the strong need for robust encapsulation. Considerable efforts have been made to fabricate solid-state or quasi-solid-state DSSCs using stable electrolytes, but most reported efficiencies have been less than 8%.[4–6,14–17] We report a high energy conversion efficiency of 8.2% at 100 mW cm^{-2}, which is one of the highest values for solid-state DSSCs (ssDSSCs) with an N719 dye.[4–6,14–17] Our process uses hierarchical double-shell nanostructures consisting of inner SnO_2 hollow spheres (SHS) surrounded by outer TiO_2 nanosheets (TNS).

One important consideration when fabricating ssDSSCs is obtaining good pore-filling of solid electrolytes into the TiO_2 films, which is strongly dependent upon the pore structure and pore size of TiO_2. For example, the energy conversion efficiency of DSSCs with well-organized TiO_2 films is much greater than those with less-organized films.[15,17] A colloidal crystal template and holographic lithography have been introduced to produce well-organized TiO_2 films with larger pores,[18] but their surface areas are too low to obtain high dye loading, resulting in low efficiency. The block copolymer-templated strategy is another effective approach for generating well-organized TiO_2 films but the synthesis of block copolymer is highly sensitive to impurities such as water and oxygen, requiring synthetic expertise and high cost.[15,19,20] The Pluronic series containing poly(ethylene oxide) (PEO) and poly(propylene oxide) (PPO) units is a relatively cheap, commercially available block copolymer, but its molecular weight is typically less than 10 000 g mol^{-1} and its segregation properties are not significant due to similar polarity between PEO and PPO units. Thus, the Pluronic series leads to smaller TiO_2 pore sizes, usually less than 10 nm, which hinders deep pore filling of large volume solid electrolytes and impedes complete crystallization while maintaining structural integrity.[15] Furthermore, organized TiO_2 films templated by block copolymers are often thin (typically less than 1 μm) due to crack formation at higher thicknesses, leading to lower efficiency.

Our group recently reported crack-free, micron-thick, organized TiO_2 films via direct self-assembly of a graft copolymer, poly(vinyl chloride)-*g*-poly(oxyethylene methacrylate) (PVC-g-POEM), and hydrophilically preformed TiO_2 nanocrystals with elongated spherical shapes. An efficiency of 7.1% was obtained from the ssDSSC using a solid polymer electrolyte.[17] Although these TiO_2 photoanodes were effective for solid electrolytes due

S. H. Ahn, D. J. Kim, W. S. Chi, J. H. Kim
Department of Chemical and Biomolecular Engineering
Yonsei University
50 Yonsei-ro, Seodaemun-gu, Seoul 120–749, Korea
E-mail: jonghak@yonsei.ac.kr

DOI: 10.1002/adfm.201400774

to larger pores and good interconnectivity, their high transparency resulted in poor light scattering properties. Thus, the preparation of organized photoanodes containing scattering centers such as hollow beads is needed to enhance light harvesting and electron collection. A shell-in-shell structure with multiple shells is considered one of the possible solutions to enhance the light scattering capabilities of a photoanode.

TiO_2 has been commonly utilized as a photoanode in DSSCs and a photocatalyst in water splitting over the last few decades.[21,22] The development of alternative metal oxides, such as ZnO, SnO_2 and Nb_2O_5, is regarded as a possible breakthrough to overcoming the low electron mobility of TiO_2. SnO_2 has been thoroughly investigated as an alternative due to its higher electron mobility and conduction band edge of 3.6 eV, which is higher than that of TiO_2 (3.2 eV).[23–25] The application of SnO_2 to DSSCs has been limited due to lower surface area, larger interfacial electron recombination and lower trapping density, leading to lower efficiency. We recently reported a one-dimensional (1D) nanostructure consisting of inner SnO_2 nanotubes (SNT) surrounded by an outer TiO_2 nanosheet (TNS), termed SNT@TNS, that provides higher surface area and suppresses electron recombination. This results in a high-efficiency ssDSSC with 7.7% at 100 mW cm^{-2}.[25]

Here, we report an ssDSSC with 8.2% improved efficiency at 100 mW/cm^2. This ssDSSC is based on hierarchical double-shell nanostructures consisting of an inner SHS surrounded by an outer TNS and is named SHS@TNS. The structure-property relationship was systematically investigated by comparing a single-shell structure with a double-shell structure, and a 1D structure (SNT@TNS) with a hollow structure (SHS@TNS) in terms of surface area, light scattering ability and electron transport. The ssDSSCs were fabricated using solid-state polymerized ionic liquid (PIL), and their performance was characterized using light transmittance, current-voltage (*J–V*) curves, incident photon to current conversion efficiency (IPCE) spectra and intensity-modulated photocurrent spectroscopy (IMPS)/intensity-modulated photovoltage spectroscopy (IMVS).

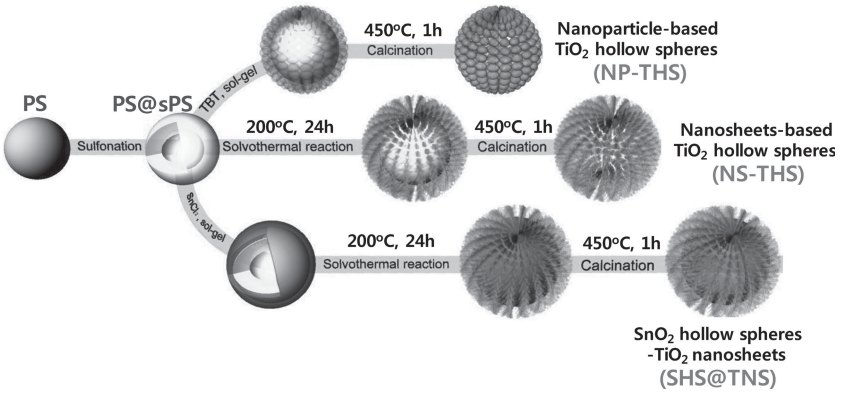

Figure 1. Schematic illustration for the preparation of nanoparticle-based TiO_2 hollow spheres (NP-THS), nanosheet-based TiO_2 hollow spheres (NS-THS) and SnO_2 hollow sphere-TiO_2 nanosheet double-shell nanostructures (SHS@TNS).

2. Results and Discussion

Nanoparticle-based TiO_2 hollow spheres (NP-THS), nanosheet-based TiO_2 hollow spheres (NS-THS) and SnO_2 hollow sphere-TiO_2 nanosheet (SHS@TNS) double-shell nanostructures were prepared by combining the processes of sol-gel and solvothermal reaction using polystyrene (PS) as a starting material, as shown in **Figure 1**. In particular, the hierarchical SHS@TNS double-shell nanostructures are effective because of their large surface area, excellent electron transport and improved light scattering abilities. First, monodisperse PS nanoparticles with a diameter of 350 nm were prepared via free-radical emulsion polymerization using azobisisobutyronitrile (AIBN) as an initiator.[26] Following sulfonation by concentrated sulfuric acid at 40 °C for 15 hours, the PS at the nanoparticle surface was converted to sulfonated polystyrene (sPS) in order to generate PS@sPS core-shell nanoparticles, as shown in **Figure 2**a. The PS@sPS core-shell nanoparticles have a pivotal role in allowing the metal oxide precursor to diffuse and grow inside the particles. This characteristic is due to the balanced heterostructure of the hydrophobic PS core and hydrophilic sPS shell. TiO_2 hollow spheres consisting of nanoparticles at the outer shell, named NP-THS, were prepared via the sol-gel method using tetrabutyl titanate (TBT) as a titania precursor, as shown in Figure 2b. Strong electrostatic bonding interactions allow sufficient, robust adsorption of TBT on the hydrophilic sPS shell.[27] This process forms NP-THS without structural deformations upon calcination at 450 °C for 1 hour. This calcination condition is appropriate for removing all organics, such as the PS or sPS template, and crystallizing TiO_2 into the anatase phase.

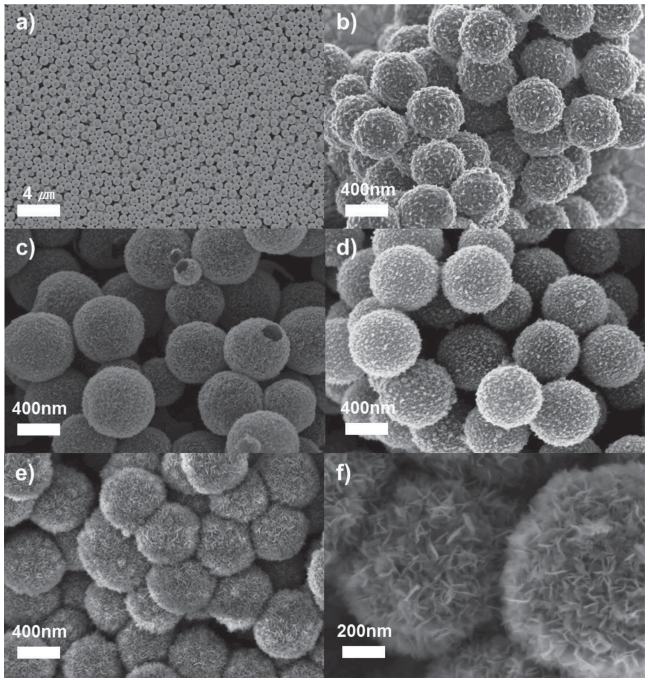

Figure 2. FE-SEM images of a) PS@sPS, b) NP-THS, c) NS-THS, d) SnO_2 hollow spheres (SHS) and e,f) SHS@TNS double-shell nanostructures.

SnO_2 hollow spheres (SHS) were also prepared in a similar way using tin(II) chloride ($SnCl_2$) as a tin precursor, as shown in Figure 2d.

To investigate the structural differences between nanoparticles and nanosheet surfaces modified by hollow spheres, nanosheet-based TiO_2 hollow spheres (NS-THS) were also prepared. A TNS layer was introduced to the sPS shell via a hydrothermal reaction followed by calcination at 450 °C, as shown in Figure 2c. Similarly, SnO_2 hollow sphere-TiO_2 nanosheet double-shell nanostructures (SHS@TNS) were prepared by introducing a TNS layer to the SHS outer surface, as shown in Figures 2e, f. Diethylenetriamine played an important role in TNS formation by facilitating electrostatic interactions between the titania precursor and the surface of the target materials, such as sPS and SnO_2.[28] The outer diameters of the hollow spheres were always greater than those of the initial PS@sPS nanoparticles, indicating complete surface modification. The largest outer diameter of a SHS@TNS double-shell nanostructure was 500 nm, indicating that a large number of nanosheets successfully covered the entire surface of the hollow spheres.

The core-shell and double-shell nanostructures of PS@sPS, NP-THS, NS-THS, SHS and SHS@TNS materials were more clearly observed using TEM measurements, as shown in **Figure 3**a-e. SHS shells were thicker than those of TiO_2-based samples such as NP-THS and NS-THS. This is due to deeper penetration of the tin precursor ($SnCl_2$) into the PS@sPS nanoparticles than the titania precursor (TBT) because the tin precursor is smaller and interacts more strongly with PS. TNS are applicable to any structure or morphology of neat materials (Figure 3f), indicating their versatility. The SHS@TNS double-shell nanostructure enhances the light scattering ability more than a single-shell structure due to its shell-in-shell structure and multireflection of incident light.[29–31] This structure also prevents SnO_2 exposure to the electrolyte, suppressing the recombination reaction between oxidized dyes and photogenerated electrons. In particular, the TNS layer is more effective at increasing the surface area in order to provide a large number of sites for higher dye loading. The 1D nanostructure with a high aspect ratio, shown in Figure 3f and Figure S1, Supporting Information, provides more efficient electron pathways than the less-organized nanoparticle-based structure. Here, the structure-property relationship was investigated in detail by comparing the 1D nanotube structure (SNT@TNS) and the hollow structure (SHS@TNS) in terms of surface area, light harvesting and electron transport.

An organized mesoporous TiO_2 (OM-TiO_2) film was employed as a matrix in which to disperse double-shell nanostructures such as SHS@TNS and SNT@TNS. The OM-TiO_2 film was prepared through direct self-assembly of the poly(vinyl chloride)-g-poly(oxyethylene methacrylate) (PVC-g-POEM) graft copolymer and hydrophilic, preformed TiO_2 nanoparticles.[17,25] As shown in **Figure 4**a, the OM-TiO_2 film showed a well-ordered mesostructure with large pores, high porosity and good interconnectivity. Such an organized structure allows for easy pore-filling of a large molecular volume polymer electrolyte into

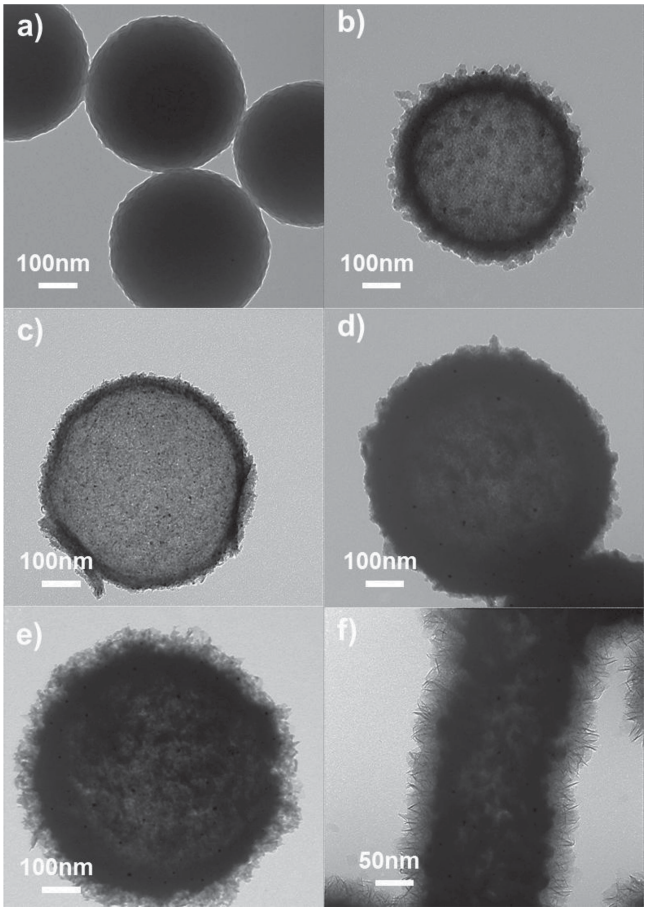

Figure 3. TEM images of a) PS@sPS, b) NP-THS, c) NS-THS, d) SHS, e) SHS@TNS double-shell nanostructures and f) SNT@TNS double-shell nanostructures.

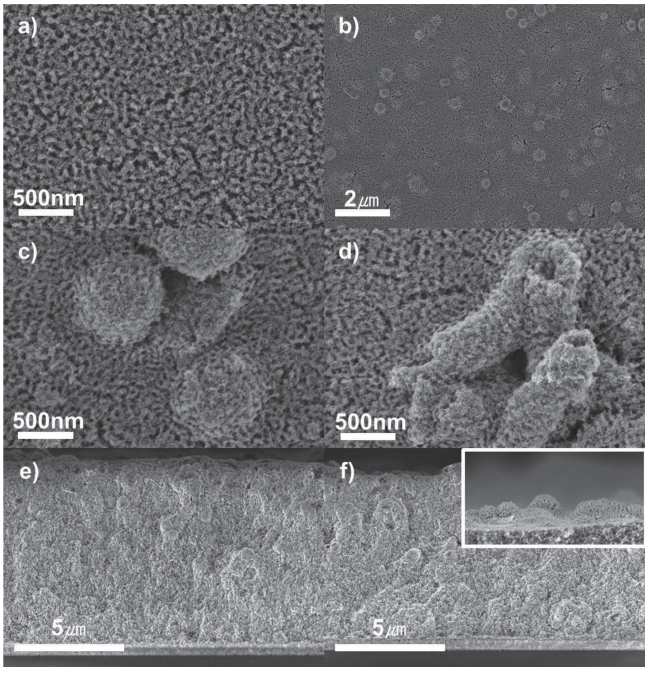

Figure 4. FE-SEM images of a) OM-TiO_2 film surface, b,c) SHS@TNS surface and d) SNT@TNS 10 wt% dispersed in OM-TiO_2 film. Cross-sectional FE-SEM images of e) NS-THS and f) SHS@TNS dispersed in OM-TiO_2 film.

the TiO_2 photoanode. The PVC-g-POEM graft copolymer works well as a structure directing agent for the synthesis of OM-TiO_2 films due to the well-defined, microphase-separated structure of hydrophobic glassy PVC main chains and the hydrophilic, rubbery POEM chains. In addition, its high molecular weight (1.1×10^5 g mol^{-1}) and amorphous nature generate large pores without disrupting the structural integrity. This facilitates deep pore-infiltration of solid electrolytes and promotes complete titania crystallization. The use of hydrophilically preformed TiO_2 nanocrystals is effective for maintaining an organized structure without crack formation at micrometer thickness. Preformed TiO_2 has selective, strong interactions with hydrophilic POEM side chains. Thus, it is preferentially confined to the POEM domains, resulting in the well-ordered mesostructure of OM-TiO_2 films.

Double-shell nanostructures, such as SHS@TNS and SNT@TNS, were uniformly dispersed in the OM-TiO_2 film without large interfacial boundaries, as shown in Figure 4b,c,d. The organized mesostructures of OM-TiO_2 were maintained and homogenized with double-shell nanostructures, indicating good interfacial contact between the nanostructures and the matrix. The relatively low density of double-shell nanostructures resulting from high porosity and empty voids inside the shell allowed for uniform distribution. To obtain the highest efficiency, the amount of double-shell nanostructures was fixed to 10 weight percent relative to the amount of preformed TiO_2. The cross-sectional images of OM-TiO_2 films with NS-THS and SHS@TNS are shown in Figure 4e, f, in which the uniform distribution of the nanostructures was more clearly observed throughout the film. There was no significant difference between the two systems, and some broken hollow spheres with voids were observed.

To verify the effect of hollow spheres and nanotubes on the surface area and pore size distribution of OM-TiO_2 films, Brunauer-Emmett-Teller (BET) surface area analysis and Barrett-Joyner-Halenda (BJH) measurements were performed, as shown in **Figure 5**a and summarized in **Table 1**. The addition of nanosheet-based materials, such as NS-THS, SHS@TNS and SNT@TNS, led to a significant increase in surface area due to the hierarchical structure of very thin nanosheets with a facet of (001). The surface area of hollow sphere-based materials, e.g., NS-THS or SHS@TNS, was greater than that of nanotube-based materials (SNT@TNS), indicating the high dye adsorption of the former, which is consistent with dye loading measurements. Double shell nanosheet-based materials, such as SHS@TNS and SNT@TNS, showed broad distributions in pore size with two maximums, indicating bimodal porosity. The first small pores were approximately 16 nm in diameter while the second large pores were 21 nm and 24 nm in diameter for SNT@TNS and SHS@TNS, respectively. Small pores provide a large surface area while the larger pores allow for easy pore-infiltration of solid polymer electrolytes. The addition of NP-THS into the OM-TiO_2 film abruptly resulted in reduced surface area from 73.5 to 68.1 m^2 g^{-1} due to the aggregation of less-organized nanoparticles to form NP-THS.

Hollow spheres with multiple shells generate high reflectivity due to multiple reflection and scattering between shells.[31,32] The ultraviolet-visible (UV-vis) diffuse reflectance of each film was analyzed to investigate the scattering abilities, as shown in Figure 5b. The reflectivity of OM-TiO_2 films improved over the entire wavelength range of 400–800 nm with the addition of nanostructures due to increased light scattering, and transparent OM-TiO_2 films changed to opaque films. The reflectivity of films with NP-THS was higher than that of those with NS-THS due to the greater shell thickness of the former, as confirmed by TEM images. The highest reflectivity was obtained from films with SHS@TNS, which is attributed to multiple reflections between the SnO_2 inner shell and TiO_2 nanosheet outer shell. The increase in reflectance was not significant for the SNT@TNS system because of small voids in tubular structures. Thus, multiple shell films containing SHS@TNS demonstrated effective reflection and scattering. This led to a significant increase of the photo response in voids comparable in size to the wavelength of visible light.

The current density-voltage (J–V) curves of ssDSSCs fabricated using OM-TiO_2-based photoanodes with various heterostructures were measured at 100 mW cm^{-2}, as shown in Figure 5c. Their photovoltaic performances are summarized in Table 1. Poly((1-(4-ethenylphenyl)methyl)-3-butyl-imidazolium iodide) (PEBII)[17,23] was synthesized through a free radical polymerization reaction and used as PIL for ssDSSCs without any additives such as I_2 or salt. The resulting PEBII film exhibited high ionic mobility with a conductivity of 2.0×10^{-4} S cm^{-1} at room temperature, as measured by two-probe method.[33] It results from the well-ordered molecular structure with π–π stacking interactions and a low glass transition temperature of –4 °C. OM-TiO_2 films templated from the self-assembly of the PVC-g-POEM graft copolymer have advantages over randomly organized films in terms of larger surface area, higher porosity and better interconnectivity between ordered blocks. As a result, the conversion efficiency of the OM-TiO_2 cell (5.7%) was greater than that of the randomly organized TiO_2 cell (4.0%) prepared with commercially available paste (Dyesol 18NR-T), mostly due to higher short-circuit current density (J_{sc}) and fill factor (FF) in the former. This demonstrates that TiO_2 photoanodes with a well-ordered structure play pivotal roles in improving the efficiency of ssDSSCs. All hybrid systems consisting of the OM-TiO_2 matrix and multi-functional nanostructures showed improved cell efficiency compared to that of neat OM-TiO_2-based cells due to a simultaneous increase in J_{sc} and open circuit voltage (V_{oc}). The conversion efficiencies of NP-THS and NS-THS cells were not significantly different from each other. This is because the V_{oc} and FF of NS-THS were slightly greater while the J_{sc} was lower than that of NP-THS cells. These properties were due to larger surface area and faster electron transport of NS-based materials, which offset the loss of light scattering. Relatively lower FF values (≈0.60) of our devices than typical a liquid electrolyte cell (≈0.70) is due to the use of solid PEBII electrolyte with large molecular volume, resulting in lower ionic conductivity and pore-filling degree than a liquid electrolyte.

Improved conversion efficiencies were obtained from devices with double shell nanostructures, i.e., SHS@TNS and SNT@TNS, even without further $TiCl_4$ treatments. This is mainly attributed to the enhanced J_{sc}, resulting from increased light scattering and electron transport. There are three major factors unique to double shell nanostructures. First, a high surface area was possible due to hierarchical structures consisting of multiple shell and TNS layers. The surface area and dye

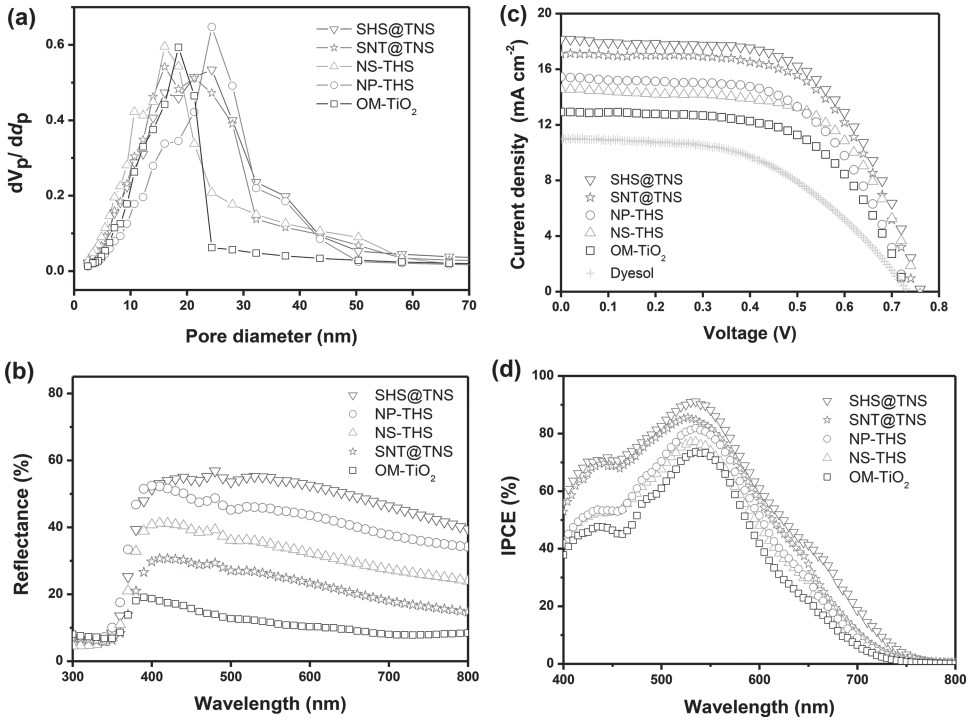

Figure 5. a) Pore size distribution of various films as determined by N_2 adsorption-desorption measurements. b) Diffuse reflectance spectra of various films. c) *J–V* curves and d) IPCE curves of ssDSSCs fabricated with various photoanodes and solid PEBII electrolyte at 100 mW cm^{-2}.

loading of SHS@TNS films were greater than those of SNT@TNS films, indicating the effectiveness of hollow sphere structures over 1D nanotube structures. Second, the higher electron mobility and larger band gap (3.8 eV) of SnO_2 compared to TiO_2 (3.2 eV), along with surface modification by TNS prevented exposure of the SnO_2 surface to the dye/electrolyte. This led to decreased interfacial electron recombination and trapping density. This study focused on reducing the size of TNS on the SnO_2 surface to minimize the partial exposure of SnO_2. This was possible by increasing the diethyltrilamine amount to double in a hydrothermal reaction. The resulting FF values of devices containing SHS@TNS or SNT@TNS were improved compared to our previous results[25] and comparable to that of neat OM-TiO_2 cells. Finally, the 1D SNT structure is effective in terms of fast electron transport but the light scattering ability of SHS is superior. Consequently, the overall efficiency of the SHS@TNS cell was higher than that of the SNT@TNS cell.

IPCE is defined as the number of electrons in the external circuit produced by an incident photon at a given wavelength. Thus, the IPCE spectrum is directly related to the J_{sc} value measured in *J–V* curves, which is in turn largely determined by dye loading, electron transfer and light scattering. The IPCE spectra of ssDSSCs with various photoanodes were measured at 100 mW cm^{-2} and are shown in Figure 5d. The IPCE values of double shell heterostructures, such as SHS@TNS or SNT@TNS, were much higher than those of neat OM-TiO_2 cells and hollow sphere cells (such as NP-THS or NS-THS). This was also verified by the *J–V* measurement results. In

Table 1. Surface area, dye loading of various photoanodes, and photovoltaic properties of ssDSSCs fabricated with various photoanodes and solid PEBII[a)] electrolyte at 100 mW/cm^2.

Photoanode[b)]	Surface area (m^2 g^{-1})[c)]	Dye loading (nmol cm^{-2})	V_{oc} (V)	J_{sc} (mA cm^{-2})	FF	η (%)
Neat OM-TiO_2	73.5	125.1	0.73	12.9	0.60	5.7
NP-THS/OM-TiO_2	68.1	120.4	0.73	15.4	0.59	6.7
NS-THS/OM-TiO_2	93.1	145.6	0.76	14.6	0.62	6.8
SHS@TNS/OM-TiO_2	92.9	147.1	0.76	18.2	0.60	8.2
SNT@TNS/OM-TiO_2	83.9	131.2	0.76	17.1	0.61	7.9
Dyesol	–	83.2	0.73	11.0	0.50	4.0

[a)]PEBII: poly(1-((4 ethenylphenyl)methyl)-3-butyl-imidazolium iodide)); [b)]NP-THS: nanoparticle-based TiO_2 hollow spheres, NS-THS: nanosheet-based TiO_2 hollow spheres, SHS@TNS: SnO_2 hollow sphere-TiO_2 nanosheet double-shell nanostructures, SNT@TNS: SnO_2 nanotube-TiO_2 nanosheet double-shell nanostructures, Dyesol: commercially available Dyesol paste (18NR-T); [c)]Determined from N_2 adsorption-desorption measurements.

particular, the SHS@TNS cell showed the greatest IPCE curves in whole regions from 400 to 750 nm, due to larger dye loading and greater light scattering. When the maximum peak of each IPCE value is normalized to 100%, as shown in Figure S2, Supporting Information, the light scattering ability of each structure is more clearly observed in longer wavelength regions. The SHS@TNS cell showed the highest normalized IPCE value from 550 to 750 nm, indicating the superior light scattering properties of multiple shells with large hollow spheres, consistent with the above reflectance results.

The dynamics of electron transport and charge device recombination were also investigated using IMPS/IMVS measurements, as shown in Figure S3, Supporting Information. A diode laser with variable power and modulation control was used as the light source for these studies. The greatest diffusion coefficient, electron lifetime and diffusion length were observed for the SNT@TNS cell, due to its 1D aligned double shell structure. The SHS@TNS cell also showed a higher diffusion coefficient, electron lifetime and diffusion length than the neat OM-TiO_2 cell and hollow sphere cells such as NS-THS or NP-THS. This demonstrates that double shell nanostructures with a highly mobile SnO_2 inner shell sufficiently minimize charge recombination.

3. Conclusion

Hierarchical SHS@TNS double-shell nanostructures with large surface area, excellent electron transport, and improved light-scattering abilities were prepared via a combined process of sol-gel and solvothermal reactions. The first step involved synthesis of 350 nm PS@sPS core-shell nanoparticles using free-radical emulsion polymerization followed by sulfonation. The second step was preparation of SHS through the electrostatic interaction of $SnCl_2$ and sPS followed by calcination at 450 °C. Finally, surface modifications of SHS with TNS were performed via solvothermal reaction at 200 °C for 24 h. This double-shell nanostructure was uniformly distributed in the OM-TiO_2 film with large pores, high porosity, and good interconnectivity due to its relatively low density resulting from high porosity and empty voids inside the shell. The existence of a SnO_2 inner shell as well as the structural differences of 1D (SNT@TNS) and hollow structures (SHS@TNS) were systematically demonstrated by *J–V* curves, IPCE, reflectance, and IMPS/IMVS results. Both double shell structures exhibited excellent ssDSSC performance, which is attributed to advantages in electron transport and light scattering abilities. The highest efficiency of 8.2%, which is one of the greatest values for N719-based ssDSSCs, was obtained from the SHS@TNS based DSSC.

4. Experimental Section

4.1. Materials

Poly(vinyl chloride) (PVC, M_n = 55,000 g mol^{-1}), poly(oxyethylene methacrylate) (POEM, poly(ethylene glycol) methyl ether methacrylate, M_n = 475 g mol^{-1}), 1,1,4,7,10,10-hexamethyltriethylene tetramine (HMTETA, 99%), copper(I) chloride (CuCl, 99%), titanium(IV) isopropoxide (TTIP, 97%), hydrogen chloride solution (HCl, 37 wt%), chloroplatinic acid hexahydrate (H_2PtCl_6), styrene (99.9%), 2,2′-azobis(2-methylpropionitrile) (AIBN), sulfuric acid (99.999%), tetrabutyl titanate (TBT, 98%), mercapto-acetic acid (98%), tin(II) chloride dihydrate (98%), urea (99%) and diethylenetriamine (99%) were purchased from Sigma-Aldrich. Tetrahydrofuran (THF), *N*-methyl pyrrolidone (NMP), methanol, 2-propanol, chloroform and acetonitrile were purchased from J. T. Baker. Deionized water (>18 MΩ m) was obtained with a water purification system made by Millipore Corporation. Ruthenium dye (535-bisTBA, N719) was purchased from Solaronix, Switzerland. Fluorine-doped tin oxide (FTO) conducting glass substrate (TEC8, 8 ohms sq^{-1}, 2.3 mm thick) was purchased from Pilkington, France. All solvents and chemical reagents used in the experiments were obtained from commercial sources as guaranteed grade reagents and used without further purification.

4.2. Preparation of PS@sPS Core-Shell Nanoparticles

Monodisperse PS spheres with a diameter of 350 nm were prepared using AIBN as an initiator. Dried PS powder (3.0 g) was immersed in 30 mL of concentrated sulfuric acid (98%), and the mixed solution was stirred at 40 °C for 15 h to form PS@sPS core-shell nanoparticles. Nanoparticles were then separated by centrifugation, washed with a large excess of ethanol and finally freeze-dried.

4.3. Preparation of NP-THS

The PS@sPS core-shell nanoparticles were immersed in a large amount of tetrabutyl titanate (TBT):alcohol (1:1 vol/vol) mixture for 8 h to allow saturated adsorption of TBT on the sPS spheres. TBT-swollen particles were separated by centrifugation, and 0.1 g of this product was dispersed into ethanol:water (1:1 vol/vol; 10 mL) and stirred at ambient temperature for 2 h to allow the sol-gel process to occur. The precipitate was collected by centrifugation, washed thoroughly with ethanol and dried at 80 °C for 12 h. Collected samples were calcinated in air at 450 °C for 1 hour to remove PS@sPS organic materials and to crystallize the titanium oxide hollow spheres.

4.4. Preparation of SHS

First, 0.2 g of PS@sPS core-shell nanoparticles was dispersed into 40 mL of 10 mM mercapto-acetic acid solution by ultrasonication for 5 min. Afterwards, 0.3 mL of concentrated hydrochloric acid, 0.5 g of tin(II) chloride dihydrate ($SnCl_2{\cdot}2H_2O$) and 0.5 g of urea were added to the above suspension. After stirring for 5 min, the reaction solution was transferred to a 150-mL flask and kept in an oil bath at 80 °C for 6 h with stirring. The precipitate was collected by centrifugation, washed thoroughly with ethanol and dried at 80 °C for 12 h. The collected samples were calcinated in air at 450 °C for 1 hour to remove PS@sPS organic materials and crystallize tin oxide hollow spheres.

4.5. Preparation of NS-THS

First, 0.1 g of PS@sPS core-shell nanoparticles was dispersed in 40 ml of isopropyl alcohol by ultrasonication for 15 min. Then, 0.3 ml of diethyltrilamine and 0.3 ml of titanium isopropoxide were added to this solution dropwise and stirred for 30 min. The solution was transferred to a 150 ml Teflon-lined autoclave, heated to 200 °C and maintained for 24 h. After the reaction, the autoclave was cooled at room temperature and the resultant was collected via centrifugation at 12 000 rpm for 30 min. The products were calcined at 450 °C in air for 1 h to obtain a highly crystalline anatase phase.

4.6. Preparation of SHS@TNS Double-Shell Nanostructure

The annealed SnO_2 HS was dispersed in 40 ml of isopropyl alcohol by ultrasonication for 15 min. Then, 0.3 ml of diethyltrilamine and 0.3 ml

of titanium isopropoxide were added to this solution dropwise and stirred for 30 min. The solution was transferred to a 150-ml Teflon-lined autoclave, heated to 200 °C and maintained for 24 h. After the reaction, the autoclave was cooled naturally at room temperature and the resultant was collected via centrifugation at 12 000 rpm for 30 min. The products were calcined at 450 °C in air for 1 h to obtain a highly crystalline phase.

4.7. Fabrication of ssDSSCs

The ssDSSCs with an active area of 0.16 cm^2 were fabricated by drop-casting polymer electrolyte solution onto the photoanode and covering with the counter electrode, following a previously reported procedure.[17,25,33–36] A dense, 100-nm-thick TiO_2 film serving as a blocking layer was prepared on the FTO glass by spin coating titanium(IV) bis(ethyl acetoacetato) diisopropoxide solution (2 wt% in butanol) at 1500 rpm for 10 s, followed by calcination at 450 °C for 30 min. The double-shell nanostructures were fully dispersed in 2 ml of tetrahydrofuran by ultrasonication for 30 min and mixed with sol-gel solution to prepare the OM-TiO_2 film. The OM-TiO_2 film was prepared via a sol-gel process using the PVC-g-POEM graft copolymer and preformed TiO_2 nanocrystals. Briefly, 0.2 g of the PVC-*g*-POEM graft copolymer was added to tetrahydrofuran solution and stirred overnight. This was followed by the addition of 0.35 g of preformed TiO_2 nanocrystals. Finally, 0.15 ml of HCl/H_2O mixture (37:63wt. ratio) was added to the solution to induce self-assembly and increase dispersion of the mixture. The viscous mixtures were deposited onto FTO glass using a doctor-blade technique, followed by sintering at 450 °C for 30 min. The organized mesoporous TiO_2 films were sensitized overnight in a $Ru(dcbpy)_2(NCS)_2$ dye (dcbpy = 2,2-bipyridyl-4,4-dicarboxylato) solution (N719, 535-bisTBA, Solaronix, 13 mg, dissolved in 50 g distilled ethanol). Pt-layered counter-electrodes were prepared by spin-coating 1 wt% H_2PtCl_6 solution in isopropanol onto the FTO glass and then sintering the film at 450 °C for 30 min. PEBII solution in acetonitrile was directly cast onto the photoanode. The photoanode and counter electrodes were then superimposed and pressed between two glass plates to achieve slow solvent evaporation and create a thin electrolyte layer. The cells were placed in a vacuum oven for 1 day to ensure complete solvent evaporation.

The DSSCs were illuminated with a Keithley Model 2400 and 1000-W xenon lamp (Oriel, 91193). The light intensity was homogeneous over an 8 × 8 in^2 area. The spectral mismatch between simulated light and natural sunlight was corrected for using a certified reference Si solar cell (Fraunhofer Institute for Solar Energy System, Mono-Si + KG filter, Certificate No. C-ISE269) for a sunlight intensity of one (100 mW cm^{-2}). This calibration was verified with an NREL-calibrated Si solar cell (PV Measurements Inc.). DSSC temperature was maintained at 25 °C throughout the measurement time using a peltier cooling apparatus. Photoelectrochemical performances were calculated with the following equations:

$$FF = \frac{V_{max} \cdot J_{max}}{V_{oc} \cdot J_{sc}} \quad (1)$$

$$\eta(\%) = \frac{V_{max} \cdot J_{max}}{P_{in}} \times 100 = \frac{V_{oc} \cdot J_{sc} \cdot FF}{P_{in}} \times 100 \quad (2)$$

where J_{sc} is short-circuit current density (mA cm^{-2}), V_{oc} is open-circuit voltage (V), P_{in} is incident light power, *FF* is fill factor, η is overall energy conversion efficiency and J_{max} (mA cm^{-2}) and V_{max} (V) are the current density and voltage in the *J–V* curve at the point of maximum power output, respectively. The photoanode active area, determined by the aperture of a black mask, was 0.16 cm^2.

The IPCE was measured as a function of wavelength from 400 to 800 nm (K3100) under short circuit conditions using the irradiation of a 300 W xenon lamp, which was obtained by a series of light filters with different wavelengths. The IPCE value was calculated using the following equation:

$$IPCE = \frac{hcI}{\lambda p} \quad (3)$$

where h and c represent Planck's constant and the speed of light in a vacuum, respectively. I is photocurrent density (mA cm^{-2}). λ and P are the wavelength (nm) and intensity (mA cm^{-2}) of the incident monochromatic light, respectively.

4.8. Characterization

The surface and cross-sectional structures of films were characterized by field emission scanning electron microscopy (FE-SEM) (SUPRA 55VP, NICEM, Carl Zeiss). After drying the sample at room temperature for one day in a vacuum oven, the specific surface area and specific pore volume of materials were measured from a N_2 adsorption-desorption isotherm via the Brunauer-Emmett-Teller (BET, for specific surface area) and Barrett-Joyner-Halenda (BJH, for specific pore volume) methods using a Belsorp-mini II device. Before collecting these measurements, the films were additionally degassed at 70 °C under dynamic vacuum (10^{-2} Torr) for 1 h. The diffuse reflectance spectra of films were acquired using a UV-visible spectrophotometer (Hewlett-Packard, Hayward, CF) over a sample area of roughly 5 × 5 μm^2 with magnification of 100. A spectral range of 300–800 nm was explored using a tungsten-halogen lamp.

4.9. Measurement of Dye Adsorption

First, N719 dye-sensitized photoanodes were dipped into 10.0 mL of a 10^{-2} M solution of NaOH in ethanol–H_2O (1:1). The mixture was stirred until the dye completely desorbed into the liquid. The volume of NaOH solution containing the fully desorbed dye was then measured by UV-visible spectroscopy. The amounts of NaOH solutions were recorded, and the absorption value at 515 nm (as a function of wavelength) was used to calculate the number of adsorbed N719 dye molecules. The Beer-Lambert law was used for calculations:

$$A = \varepsilon lc \quad (4)$$

where A is absorbance of the UV-visible spectra at 515 nm, ε = 14 100 M^{-1} cm^{-1} is the molar extinction coefficient of the dye at 515 nm, l is the path length of the light beam, and c is the dye concentration.

Supporting Information

Supporting Information is available from the Wiley Online Library or from the author.

Acknowledgements

We acknowledge the financial support of a grant from the National Research Foundation (NRF) funded by the Korean government (MEST) through the Active Polymer Center for Pattern Integration (2007-0056091), the Core Research Program (2012R1A2A2A02011268) and the Korea Center for Artificial Photosynthesis (KCAP) (2009-0093883).

Received: March 9, 2014
Published online: May 23, 2014

[1] B. O'Regan, M. Gratzel, *Nature* **1991**, *353*, 737.
[2] C.-Y. Chen, J.-G. Chen, S.-J. Wu, J.-Y. Li, C.-G. Wu, K.-C. Ho, *Angew. Chem. Int. Edn.* **2008**, *47*, 7342.

[3] H.-P. Wu, Z.-W. Ou, T.-Y. Pan, C.-M. Lan, W.-K. Huang, H.-W. Lee, N. M. Reddy, C.-T. Chen, W.-S. Chao, C.-Y. Yeh, E. W.-G. Diau, *Energy Environ. Sci.* **2012**, *5*, 9843.
[4] S. Yanagida, Y. H. Yu, K. Manseki, *Acc. Chem. Res.* **2009**, *42*, 1827.
[5] J. Xia, N. Masaki, M. Lira-Cantu, Y. Kim, K. Jiang, S. Yanagida, *J. Am. Chem. Soc.* **2008**, *130*, 1258.
[6] H. Wang, X. Zhang, F. Gong, G. Zhou, Z. S. Wang, *Adv. Mater.* **2012**, *24*, 121.
[7] K.-C. Huang, Y.-C. Wang, R.-X. Dong, W.-C. Tsai, K.-W. Tsai, C.-C. Wang, Y.-H. Chen, R. Vittal, J.-J. Lin, K.-C. Ho, *J. Mater. Chem.* **2010**, *20*, 4067.
[8] F. Sauvage, D. H. Chen, P. Comte, F. Z. Huang, L. P. Heiniger, Y. B. Cheng, R. A. Caruso, M. Graetzel, *ACS Nano* **2010**, *4*, 4420.
[9] D. H. Chen, F. Z. Huang, Y. B. Cheng, R. A. Caruso, *Adv. Mater.* **2009**, *21*, 2206.
[10] B. Lee, D. B. Buchholz, R. P. H. Chang, *Energy Environ. Sci.* **2012**, *5*, 6941.
[11] H. Wang, Y. H. Hu, *Energy Environ. Sci.* **2012**, *5*, 8182.
[12] Q. D. Tai, B. L. Chen, F. Guo, S. Xu, H. Hu, B. Sebo, X. Z. Zhao, *ACS Nano* **2011**, *5*, 3795.
[13] W. Wei, H. Wang, Y. H. Hu, *J. Mater. Chem. A* **2013**, *1*, 14350.
[14] C. Xu, J. Wu, U. V. Desai, D. Gao, *Nano Lett.* **2012**, *12*, 2420.
[15] P. Docampo, S. Guldin, M. Stefik, P. Tiwana, M. C. Orilall, S. Huttner, H. Sai, U. Wiesner, U. Steiner, H. J. Snaith, *Adv. Funct. Mater.* **2010**, *20*, 1787.
[16] J. K. Koh, J. Kim, B. Kim, J. H. Kim, E. Kim, *Adv. Mater.* **2011**, *23*, 1641.
[17] S. H. Ahn, W. S. Chi, J. T. Park, J. K. Koh, D. K. Roh, J. H. Kim, *Adv. Mater.* **2012**, *24*, 519.
[18] S. Colodrero, A. Forneli, C. Lopez-Lopez, L. Pelleja, H. Miguez, E. Palomares, *Adv. Funct. Mater.* **2012**, *22*, 1303.
[19] E. J. W. Crossland, M. Nedelcu, C. Ducati, S. Ludwigs, M. A. Hillmyer, U. Steiner, H. J. Snaith, *Nano Lett.* **2009**, *9*, 2813.
[20] S. Guldin, S. Huettner, P. Tiwana, M. C. Orilall, B. Uelguet, M. Stefik, P. Docampo, M. Kolle, G. Divitini, C. Ducati, S. A. T. Redfern, H. J. Snaith, U. Wiesner, D. Eder, U. Steiner, *Energy Env. Sci.* **2011**, *4*, 225.
[21] Y. H. Hu, *Angew. Chem. Int. Ed.* **2012**, *51*, 12410.
[22] Y. H. Hu, *Adv. Mater.* **2014**, *26*, 2102.
[23] K. Park, Q. F. Zhang, B. B. Garcia, X. Y. Zhou, Y. H. Jeong, G. Z. Cao, *Adv. Mater.* **2010**, *22*, 2329.
[24] J. F. Qian, P. Liu, Y. Xiao, Y. Jiang, Y. L. Cao, X. P. Ai, H. X. Yang, *Adv. Mater.* **2009**, *21*, 3663.
[25] S. H. Ahn, D. J. Kim, W. S. Chi, J. H. Kim, *Adv. Mater.* **2013**, *25*, 4893.
[26] Z. Z. Yang, Z. W. Niu, Y. F. Lu, Z. B. Hu, C. C. Han, *Angew. Chem. Int. Edn.* **2003**, *42*, 1943.
[27] S. J. Ding, D. Y. Zhang, H. B. Wu, Z. C. Zhang, X. W. Lou, *Nanoscale* **2012**, *4*, 3651.
[28] J. S. Chen, D. Y. Luan, C. M. Li, F. Y. C. Boey, S. Z. Qiao, X. W. Lou, *Chem. Commun.* **2010**, *46*, 8252.
[29] S. J. Ding, J. S. Chen, X. W. Lou, *Adv. Funct. Mater.* **2011**, *21*, 4120.
[30] P. Si, S. J. Ding, J. Yuan, X. W. Lou, D. H. Kim, *ACS Nano* **2011**, *5*, 7617.
[31] L. L. Liang, Y. M. Liu, C. H. Bu, K. M. Guo, W. W. Sun, N. Huang, T. Peng, B. Sebo, M. M. Pan, W. Liu, S. S. Guo, X. Z. Zhao, *Adv. Mater.* **2013**, *25*, 2174.
[32] W. Q. Fang, X. H. Yang, H. J. Zhu, Z. Li, H. J. Zhao, X. D. Yao, H. G. Yang, *J. Mater. Chem.* **2012**, *22*, 22082.
[33] W. S. Chi, J. K. Koh, S. H. Ahn, J.-S. Shin, H. Ahn, D. Y. Ryu, J. H. Kim, *Electrochem. Commun.* **2011**, *13*, 1349.
[34] S. H. Ahn, W. S. Chi, D. J. Kim, S. Y. Heo, J. H. Kim, *Adv. Funct. Mater.* **2013**, *23*, 3901.
[35] J. T. Park, W. S. Chi, D. K. Roh, S. H. Ahn, J. H. Kim, *Adv. Funct. Mater.* **2013**, *23*, 26.
[36] D. K. Roh, W. S. Chi, H. Jeon, S. J. Kim, J. H. Kim, *Adv. Funct. Mater.* **2014**, *24*, 379.